Dirac nodal line in hourglass semimetal Nb_3SiTe_6

Ro-Ya Liu[1,2,3,4,5]*, Angus Huang[6], Raman Sankar[3], Joseph Andrew Hlevyack[1,2], Chih-Chuan Su[3], Shih-Chang Weng[5], Meng-Kai Lin[1,2], Peng Chen[7], Cheng-Maw Cheng[5], Jonathan D. Denlinger[4], Sung-Kwan Mo[4], Alexei V. Fedorov[4], Chia-Seng Chang[3], Horng-Tay Jeng[3,6,8]*, Tien-Ming Chuang[3], Tai-Chang Chiang[1,2]*

[1] *Department of Physics, University of Illinois at Urbana-Champaign, Urbana, Illinois 61801, USA.*

[2] *Frederick Seitz Materials Research Laboratory, University of Illinois at Urbana-Champaign, Urbana, Illinois 61801, USA.*

[3] *Institute of Physics, Academia Sinica, Taipei, 11529, Taiwan.*

[4] *Advanced Light Source, Lawrence Berkeley National Laboratory, Berkeley, CA 94720, USA.*

[5] *National Synchrotron Radiation Research Center, Hsinchu 30076, Taiwan.*

[6] *Department of Physics, National Tsing Hua University, Hsinchu, 30013, Taiwan.*

[7] *Key Laboratory of Artificial Structures and Quantum Control (Ministry of Education), Shenyang National Laboratory for Materials Science and Shanghai Center for Complex Physics, School of Physics and Astronomy, Shanghai Jiao Tong University, Shanghai 200240, China*

[8] *Physics Division, National Center for Theoretical Sciences, Taipei 10617, Taiwan.*

Corresponding authors:

*Tai-Chang Chiang, Email: tcchiang@illinois.edu

*Ro-Ya Liu, Email: liu.roya@nsrrc.org.tw

*Horng-Tay Jeng, Email: jeng@phys.nthu.edu.tw

ABSTRACT: Glide-mirror symmetry in nonsymmorphic crystals can foster the emergence of novel hourglass nodal loop states. Here, we present spectroscopic signatures from angle-resolved photoemission of a predicted topological hourglass semimetal phase in Nb_3SiTe_6. Linear band crossings are observed at the zone boundary of Nb_3SiTe_6, which could be the origin of the nontrivial Berry phase and are consistent with a predicted glide quantum spin Hall effect; such linear band crossings connect to form a nodal loop. Furthermore, the saddle-like Fermi surface of Nb_3SiTe_6 observed in our results helps unveil linear band crossings that could be missed. *In situ* alkali-metal doping of Nb_3SiTe_6 also facilitated the observation of other band crossings and parabolic bands at the zone center correlated with accidental nodal loop states. Overall, our results complete the system's band structure, help explain prior Hall measurements, and suggest the existence of a nodal loop at the zone center of Nb_3SiTe_6.

KEYWORDS: Hourglass fermions, Dirac nodal loop, nonsymmorphic crystals, glide-mirror symmetry, photoemission, first-principles band structures

Topology in condensed-matter systems has emerged as a fundamental avenue for realizing exotic symmetry-protected Dirac fermions and emergent phases with unconventional but technologically relevant electronic properties, including topological insulators, topological crystalline insulators, and topological superconductors[1,2,3,4,5,6]. From initial theoretical discussions regarding the intimate connection between massless Dirac surface states and their topological protection due to time-reversal symmetry, particle-hole symmetry, etc.[7], the theoretical and experimental focuses have now blossomed into considerations of unusual—albeit versatile—fermion states that arise due to certain crystal point group symmetries[5,6] , even those that are protected by a nonsymmorphic space group[8,9]. Indeed, in the presence of certain crystalline symmetries, the Dirac fermion states may cross to form a Dirac point or generate a manifold Dirac nodal point, a Dirac nodal curve, or a Dirac nodal loop in *k*-space[6,10,11,12], and electrons' behaviors near a manifold Dirac point have been classified, for example, as Weyl fermion[6,10], hourglass fermion[11], and wallpaper fermion[12]. However, though numerous compounds have been predicted to host topological nodal lines or nodal loops[13], recent experimental works via angle-resolved photoemission spectroscopy (ARPES) of these topological quasiparticle band dispersions have mainly focused on just a few isostructural families, such as transition metal monopnictides[14,15,16], ZrSiS and others in the PbFCl-type family[17,18,19,20,21,22], and $PbTaSe_2$[13], rendering the physical picture of most topological nodal line semimetals largely incomplete.

Particularly, hourglass fermions are among the newest types of nodal fermions expected to emerge in topological nodal line semimetals possessing glide-mirror symmetry[11,23]. In such materials, the partner switching of eigenstates between certain time-reversal invariant momenta (TRIM), as required by mirror and glide-mirror symmetries, causes so-called "hourglass-like" band dispersions to arise with a fourfold-degenerate nodal point, which connects with other nodal points to form a closed and topologically protected Dirac loop in *k*-space[23]. Prior experimental results have confirmed the existence of hourglass fermions in KHgSb[24], but their presence has also been predicted in the orthorhombic family of X_3SiTe_6 (X = Ta, Nb) crystals[23, 25], wherein the hourglass bands are robust under the spin-orbit interaction[23]. Nevertheless, while prior ARPES studies have focused on probing one-dimensional massless Dirac fermions in the related $NbSi_{0.45}Te_2$ compound[26] as well as nodal lines and their relation to hourglass fermions in Ta_3SiTe_6[27], a comprehensive survey of the electronic band structure of Nb_3SiTe_6—one that considers hourglass bands that disperse with respect to the momentum k_z along the direction normal to the crystal's surface—is still lacking.

In this work, by combining density functional theory (DFT) calculations together with high-resolution ARPES, we have carefully performed a systematic study of the electronic band structure of the hourglass semimetal candidate Nb_3SiTe_6. By conducting mappings with respect to the momentum k_z parallel to the crystal's surface normal, we have observed a downward dispersing band near the Fermi level that is the lower part of hourglass fermion bands, as

inferred from our DFT calculations. The observed band shapes strongly support Nb_3SiTe_6 as an hourglass semimetal candidate. Moreover, our careful k_z band mappings indicate that the nodal line associated with these hourglass dispersions is periodic every two Brillouin zones (BZs), as verified by our DFT calculations of the spectral function. Also, a saddle-like Fermi surface has been mapped, which supports prior evidence from transport[28,29,30,31] for the dominance of hole carriers in the system's electronic properties. Lastly, *in situ* K doping of Nb_3SiTe_6 during ARPES facilitated the examination of other band crossings and parabolic bands at the zone center that are associated with nodal loop dispersions. Our results not only provide compelling indications of hourglass fermions in Nb_3SiTe_6 but also suggest that these hourglass fermions must figure prominently in the physics of Nb_3SiTe_6 by virtue of their proximity to the system's Fermi level, rendering Nb_3SiTe_6 an intriguing candidate for topological device applications.

As shown in Fig. 1(a), the orthorhombic unit cell for Nb_3SiTe_6 consists of two van-der-Waals-bonded layers, each of which contains a Nb-Si atomic sheet sandwiched in between two puckered-hexagonal atomic layers of Te. The stacking between the unit cell's component layers is of the AB-type. That is, the four Te layers are in an AABB stacking pattern along the (001) direction of the unit cell, suggestive of the system's glide mirror symmetry. The bulk lattice is assembled by vertically stacking many unit cells on top of one another with van der Waals bonding between layers. For reference, Fig. 1(b) displays the orthorhombic bulk

BZ along with its (001)-projected surface BZ with key high-symmetry points indicated. Topographic images of *in situ* cleaved Nb_3SiTe_6 single crystals, as obtained from scanning tunneling microscopy (STM), confirmed both the atomic structure and high crystallinity of the probed surfaces [Fig. 1(c)]. First-principles calculations of the bulk band structure for Nb_3SiTe_6 [see Fig. 1(d)] yield two hourglass-like band dispersions near $E = 0$ eV and $E =$ -0.4 eV [marked as α and γ, respectively, in Fig. 1(d)], which correspond to two pairs of hourglass fermions. Near the zone center, another set of bands with a nodal loop dispersion is evident along ΓY in the theoretical band structure [identified as β in Fig. 1(d)], whose lower half converges at the zone center to form a saddle-like surface in energy-momentum space [labelled as s in Fig. 1(d)]; the gap opening in these hourglass bands is due to glide-mirror symmetry breaking. The Fermi surface of Nb_3SiTe_6 itself is generally saddle-shaped with a local minimum along ΓY and a local maximum along ΓX [Fig. 1(e)], and the hourglass fermion band crossings along XS [identified as α and γ in Fig. 1(d)] connect to form a Dirac nodal loop in *k*-space in the XSRU plane, centered about the zone boundary point S [see Fig. 1(f)].

Representative ARPES results for the valence band structure of Nb_3SiTe_6 are summarized in Fig. 2. In Fig. 2(a), the Fermi surface contour map, taken over multiple BZs, displays a dumbbell-shaped contour centered about the zone center and with its long axis oriented along $\overline{\Gamma Y}$, while another open contour centered about the $\overline{X}$ point arches along the zone boundary; the latter contour should be associated with a topological nodal line, as in Ta_3SiTe_6[27]. Clearly,

though the intensities of Fermi surface contours decrease markedly outside of the first BZ (FBZ) and are likely modulated by complex matrix element effects and photon-energy-dependent (k_z-dependent) cross sections[32], such contours are nevertheless sharp and display a clear periodic pattern in k space over multiple BZs, indicative of the high single crystallinity of the measured Nb_3SiTe_6 sample [Fig. 2(a)], as confirmed by our X-ray diffraction results (see Supporting Information). Particularly, the dumbbell-shaped contour in the FBZ continuously connects with that of the next BZ along $\overline{\Gamma Y}$.

Select momentum cuts through these dumbbell-shaped Fermi surface contours [Fig. 2(a)] at strategically chosen k_x and k_y, where k_x and k_y are momentum components parallel to $\overline{\Gamma X}$ and $\overline{\Gamma Y}$, respectively, provide further support for both the periodicity and anisotropy of the system's electronic band structure, while illustrating rich photoemission matrix element effects in the measured band dispersions [Figs. 2(b)–2(e) and 3(a)]. Indeed, though ARPES intensities of states near the Fermi level in the FBZ are too intense for resolving band features [cuts 1 and 3, e.g., $k_x = k_y = 0$ Å^{-1}, in Figs. 2(b) and 2(d)], k-space cuts taken away from the sample's normal in other Brillouin zones [cuts 2 and 4, e.g., $k_x = 0.96$ Å^{-1} and $k_y = -0.52$ Å^{-1}, in Figs. 2(c) and 2(e)] are highly illuminating: For cut 2 parallel to $\overline{\Gamma Y}$ [Fig. 2(c)], two parabolic bands opening upwards—a small one with its minimum at $E = \sim$-0.02 eV and another spanning the energy range $E = 0$ to -0.2 eV—are repeatedly observable at the zone centers of multiple Brillouin zones [see Fig. 2(c) from $k_y = -0.78$ to -1.82 Å^{-1}]; however, for cut 4 parallel

to $\overline{\Gamma X}$ [Fig. 2(e)], a large, holelike band centered about the zone center and with its apex at E = ~-0.02 eV is instead discernible. These two results thus reveal a saddle-like surface in energy-momentum space, with its saddle point at the zone center at E = ~-0.02 eV, as well as the dominance of holelike carriers to the crystal's electronic properties, consistent with the theoretical band structure [refer to bands marked by blue arrows in Fig. 1(d)] and prior observations from transport and the system's thermoelectric properties[28,29,30,31]. Nevertheless, the predicted energy position of the saddle point is deeper in energy (at E = ~-0.1 eV) than that observed in these measurements (at E = ~-0.02 eV), likely attributable to slight doping of the Nb_3SiTe_6 crystal during its synthesis.

Furthermore, the observation of this saddle-like surface is inherently tied to potential signatures of hourglass dispersions gapped by spin-orbit coupling (SOC) near the zone center of Nb_3SiTe_6[23], per our theoretical and experimental band structure comparisons [Figs. 1(d) and 3(a)–3(c)]. Like Fig. 2(c) but now overlaid with theoretical band structures, Fig. 3(a) displays the band mapping for cut 2 indicated in the Fermi surface map of Fig. 2(a) (with k_x = 0.96 Å^{-1}), which is the cleanest cut parallel to $\overline{\Gamma Y}$ for observing and confirming the periodicity of one of the saddle-shaped surface's bands over multiple BZs [blue arrow in Fig. 3(a)]. Figures 3(b) and 3(c) summarize two-dimensional (2D) curvature results for ARPES spectra measured along $\overline{\Gamma Y}$ in the FBZ before and after *in situ* alkali doping, each superimposed with the associated DFT calculations of pure Nb_3SiTe_6 [33]. The results before and after alkali metal

doping are quite clear [compare Figs. 3(b) and 3(c)]: Aside from effectively shifting all bands to deeper binding energies, alkali metal doping of the Nb_3SiTe_6 surface facilitates further identification of band features likely related to nodal loop bands [green arrow in each of Figs. 3(a) and 3(c)], namely, one giving rise to a band crossing at the $\overline{Y}$ point [red arrow in Fig. 3(c)] and also the upward opening parabolic band of the saddle-like surface [blue arrow in each of Fig. 3(a) and 3(c)]. The photoemission intensity of the former is largely suppressed in the pristine case [Fig. 3(b)] but is visible in the alkali-doped system [red arrow in Fig. 3(c)], likely due to complex photoelectron diffraction effects and cross section variations of the probed bands. Overall, though the complete band dispersions of the hourglass fermions gapped by SOC are inaccessible through photoemission based upon our theoretical and experimental analysis, there is nevertheless evidence for nodal loop band dispersions located very close to the Fermi level [Figs. 3(a)–3(c)][23], which have yet to be considered in the physics of hourglass semimetals and related systems[24,26,27].

Besides candidate gapped hourglass bands close to the zone center, two other species of hourglass subbands with linear, Dirac-like dispersions near the BZ boundaries also appear in our ARPES data—one set very close to the Fermi level, the other buried at deeper binding energies from E = -0.4 to -0.6 eV [Figs. 1(d), 2(e), and 4(a)–4(c)]. A schematic diagram showing the relationships of these linear dispersions (along ΓX) to their partner hourglass band crossings (on the XS k-path) is displayed in Fig. 4(a). Evidently, like the presumed nodal loop

bands of the saddle-like surface, the ARPES intensities of these linear bands exhibit marked photoemission matrix element effects, as captured by their modulations across the BZ in the constant energy contour maps [Fig. 2(b)] and left-right intensity asymmetry in the band mappings [Figs. 2(d), 2(e), and 4(c)]. All linear dispersions here are spin-polarized [schematically indicated by thin aqua and blue arrows in Fig. 4(b)], as shown in the related hourglass fermion system KHgSb[11,24] and further unveiled in our theoretical calculations of each linear band's spin texture (with spin projection taken along the k_y-direction or parallel to $\overline{\Gamma Y}$) [Fig. 4(d)]. (See also Section 5 in the Supporting Information.) Specifically, for each Dirac-like point, the two partner bands possess opposite spin polarizations relative to one another, which all taken together contribute no net current flow over the BZ[11]. Consequently, such hourglass systems have been dubbed glide-symmetric analogs of the quantum spin Hall (QSH) state—or more aptly, so-called double QSH systems per the two species of linear band crossings [Figs. 4(b) and 4(c)][11,24,34]. Thus far, experimental signatures of a double QSH state have only appeared in transport measurements of KHgSb[34] but clearly, in the case of Nb_3SiTe_6, our theoretical calculations of spin textures around the $\overline{X}$ point now also suggest that Nb_3SiTe_6 is a candidate double QSH system [Fig. 4(d)].

However, in Nb_3SiTe_6, the two sets of linear bands also exhibit distinct, divergent behaviors in their spin polarizations [Fig. 4(d)] (see Section 5 in the Supporting Information): For bands at deeper binding energies [aqua arrows in Figs. 4(b) and 4(c)], the linear dispersions

exhibit strong spin polarization, while for those nearest the Fermi level [blue arrows in Figs. 4(b) and 4(c)], there exists two subbands with an energy splitting of ~20 meV and very closely spaced spin-polarized bands near the Fermi level, though all linear subbands here are more clearly spin-polarized at deeper binding energies (starting from E ~ -0.075 eV). Therefore, due to the expected small energy splitting between subbands and the marked superpositions of spin polarizations near the Fermi level around the $\overline{\mathrm{X}}$ points, a spin-resolved transport measurement might be unable to identify a clear double QSH state in Nb_3SiTe_6. Nevertheless, this observation certainly does not discount the importance of these linear band crossings to the system's nontrivial band topology[23]. Indeed, in a recent transport study of Nb_3SiTe_6, a nontrivial Berry phase has been found via Shubnikov-de Haas oscillation measurements[30], which can be readily attributed to the linear subbands of the hourglass fermions and their unusual spin textures about the $\overline{\mathrm{X}}$ points. Spin-resolved ARPES measurements would be helpful for probing the spin textures of these linear subbands in the future.

Lastly, because the band structure of Nb_3SiTe_6 should exhibit dispersion along the k_z-direction or the surface normal direction, as evidenced by the predicted hourglass bands along the XS k-path [Fig. 1(f)], band mappings under varying incident photon energy were undertaken to directly probe hourglass fermions' band dispersions in Nb_3SiTe_6. As revealed in the Fermi surface mapping in the k_x-k_z plane [Fig. 4(e)], where k_x and k_z are momentum components parallel to the $\overline{\Gamma\mathrm{X}}$ and [001] directions, respectively, the linear subbands nearest

the Fermi level at the $\overline{\mathrm{X}}$ point [Figs. 4(a)–4(d)] give rise to a continuous line along XS, though the photoemission intensity itself varies but peaks every 2 BZs [Fig. 4(e)]. These periodic intensity variations are attributable to the weak van der Waals bonding between neighboring Nb_3SiTe_6 layers, consistent with prior findings from ARPES mappings of the related hourglass semimetal Ta_3SiTe_6[27]. Moreover, this periodicity is readily captured in our theoretical spectral function of Nb_3SiTe_6 along XS calculated over multiple BZs, once DFT results are unfolded according to the BZ of 1*T* $NbTe_2$ [Fig. 5(a)]. Such experimental and theoretical results suggest that the spectral weights of hourglass bands near the Fermi level [nodal point indicated by a red arrow in Fig. 5(a)] should vary periodically every 2 BZs [Figs. 4(e) and 5(a)].

Furthermore, since the energy splitting between hourglass bands near the Fermi level is often very small [~20–50 meV, per Figs. 1(d) and 5(a)], 2D curvature data processing[33] of k_z-dependent band mappings around the $\overline{\mathrm{X}}$ point was employed to search for hourglass bands with characteristic dispersions along the XS *k*-path [Figs. 5(b)–5(g)]. As shown in Figs. 5(b) and 5(c), 2D curvature band mappings along XS exhibit a downward dispersing band with an apex at the S point, which corresponds quite well with an hourglass band found in the theoretical data [Fig. 5(a)]; the experimental results confirm that only half of the hourglass-like structure is accessible by photoemission [Figs. 5(a)–5(c)]. Even so, although the hourglass nodal point near $E = \sim 0$ eV is not discernible in the measured mappings [compare Fig. 5(a) to Figs. 5(b) and 5(c)], the observed downward band is certainly direct evidence for

hourglass physics [Figs. 5(a)–5(c)] and importantly a Dirac nodal curve in Nb_3SiTe_6, as confirmed by 2D curvature mappings around the $\overline{X}$ point taken along $\overline{\Gamma X}$ at judiciously chosen k_z [Figs. 5(d)–5(g)]. Undoubtedly, the apex of the Dirac-like band crossing structure near the Fermi level varies as a function of k_z, shifting by about ~+20 meV (~-20 meV) to lower (higher) binding energies as k_z is continuously tuned from the X to S (S to X) points [Figs. 5(b)–5(g)]. While Ta_3SiTe_6 and the related system $NbSi_{0.45}Te_2$ have been measured very recently by ARPES[26,27], this Dirac nodal curve along XS and more generally all dispersions along XS of X_3SiTe_6 (X = Ta, Nb) have not been reported yet[26,27]. However, the strongest and most direct evidence for hourglass physics in Nb_3SiTe_6 is provided by studying bands along XS, as in Figs. 4(e)–5(g).

Altogether, our comprehensive photoemission and theoretical study of bulk Nb_3SiTe_6 single crystal provides direct evidence for the existence of hourglass fermions as well as unconventional spin textures in Nb_3SiTe_6. Specifically, the observation of a saddle-shaped surface in the measured band mappings and Fermi surface supports the existence of nodal loop dispersions near the zone center, in corroboration with prior transport works[28]. Additionally, the identification of two species of Dirac-like, linear band crossings at the $\overline{X}$ point, together with their theoretical spin-resolved band structures, support a scenario for an exotic double QSH state in Nb_3SiTe_6, previously only discovered in the hourglass semimetal KHgSb[34]. Furthermore, our photon-energy-dependent or k_z-dependent mappings along XS—never

undertaken in any ARPES work on the orthorhombic family of X_3SiTe_6 (X = Ta, Nb) single crytals[26,27]—have unveiled an hourglass band that is a Dirac nodal curve, based upon our DFT results and experimental data. Though only half of an hourglass-like structure is accessible through photoemission, the k_z-dependent band maps nonetheless suggest that hourglass fermions must contribute to the electronic properties of Nb_3SiTe_6 due to the proximity of their band structures near the Fermi level. All in all, our work not only provides future impetus in the identification of even more unusual topological materials but also identifies Nb_3SiTe_6 as a candidate system harboring unconventional spin textures accessible to spintronic applications.

ASSOCIATED CONTENT

Supporting Information: Additional information about the sample preparation, the experimental setup, the DFT calculation details, XRD measurement, XPS measurement, and spin-resolved DFT calculations.

AUTHOR INFORMATION

Corresponding Authors

*Correspondence to: Ro-Ya Liu (liu.roya@nsrrc.org.tw), Horng-Tay Jeng (jeng@phys.nthu.edu.tw), and T.-C. Chiang (tcchiang@illinois.edu)

Author Contributions

RYL, MKL, PC, and JAH performed ARPES measurements at the ALS or NSRRC, where JD and CMC provided technical help during beamline operations. AH and HTJ performed theoretical calculations. RS synthesized the single crystal. SCW performed XRD measurements. CCS and TMC performed STM measurements. RYL and TCC analyzed the data, interpreted the results, and wrote the first draft. All coauthors contributed to discussions and improvements that led to the final version of the manuscript.

ACKNOWLEDGEMENTS

This work is supported by the U.S. Department of Energy, Office of Science, Office of Basic Energy Sciences, Division of Materials Science and Engineering, under Grant No. DE-FG02-07ER46383 (T.C.C.). This research used resources of the Advanced Light Source, a U.S. DOE Office of Science User Facility under contract no. DE-AC02-05CH11231. H.T.J acknowledges support from the Ministry of Science and Technology, Taiwan, under grant MOST 109-2112-M-007-034-MY3 and from NCHC, CINC-NTU, and CQT-NTHU-MOE, Taiwan. P.C. acknowledges support from the Science and Technology Commission of Shanghai Municipality under Grant No. 21JC1403000 and sponsorship from Yangyang Development Fund. R. S. is supported by Ministry of Science and Technology of Taiwan (MOST110-2124-M-001-009-MY3) and (MOST-110-2112-M-001-065-MY3). R.S., H.T.J and T.M.C acknowledge support from Academia Sinica (AS-iMATE-111–12). R.Y.L.

acknowledges support from the Ministry of Science and Technology of Taiwan under Grant No. MOST 111-2112-M-213-010-MY3.

REFERENCES

(1) Fu, L.; Kane, C. L.; Mele, E. J.Topological Insulators in Three Dimensions. *Phys. Rev. Lett.* **2007**, *98* (10), 106803.

(2) *Topological Matter*; Bercioux, D., Cayssol, J., Vergniory, M. G., Reyes Calvo, M., Eds.; Springer Series in Solid-State Sciences; Springer International Publishing: Cham, 2018; Vol. 190.

(3) Fu, L.Topological Crystalline Insulators. *Phys. Rev. Lett.* **2011**, *106*, 106802.

(4) Shiozaki, K.; Sato, M.Topology of Crystalline Insulators and Superconductors. *Phys. Rev. B* **2014**, *90*, 165114.

(5) Liu, Z. K.; Zhou, B.; Zhang, Y.; Wang, Z. J.; Weng, H. M.; Prabhakaran, D.; Mo, S. K.; Shen, Z. X.; Fang, Z.; Dai, X.; Hussain, Z.; Chen, Y. L.Discovery of a Three-Dimensional Topological Dirac Semimetal, Na_3Bi. *Science* **2014**, *343* (6173), 864–867.

(6) Lin, C.-L.; Arafune, R.; Liu, R.-Y.; Yoshimura, M.; Feng, B.; Kawahara, K.; Ni, Z.; Minamitani, E.; Watanabe, S.; Shi, Y.; Kawai, M.; Chiang, T.-C.; Matsuda, I.; Takagi, N.Visualizing Type-II Weyl Points in Tungsten Ditelluride by Quasiparticle Interference. *ACS Nano* **2017**, *11*, 11459–11465.

(7) Schnyder, A. P.; Ryu, S.; Furusaki, A.; Ludwig, A. W. W.Classification of Topological

Insulators and Superconductors in Three Spatial Dimensions. *Phys. Rev. B - Condens. Matter Mater. Phys.* **2008**, *78*, 195125.

(8) Shiozaki, K.; Sato, M.; Gomi, K.Topology of Nonsymmorphic Crystalline Insulators and Superconductors. *Phys. Rev. B* **2016**, *93*, 195413.

(9) Alexandradinata, A.; Wang, Z.; Bernevig, B. A.Topological Insulators from Group Cohomology. *Phys. Rev. X* **2016**, *6* (2), 021008.

(10) Feng, B.; Chan, Y. H.; Feng, Y.; Liu, R. Y.; Chou, M. Y.; Kuroda, K.; Yaji, K.; Harasawa, A.; Moras, P.; Barinov, A.; Malaeb, W.; Bareille, C.; Kondo, T.; Shin, S.; Komori, F.; Chiang, T. C.; Shi, Y.; Matsuda, I.Spin Texture in Type-II Weyl Semimetal WTe_2. *Phys. Rev. B* **2016**, *94*, 195134.

(11) Wang, Z.; Alexandradinata, A.; Cava, R. J.; Bernevig, B. A.Hourglass Fermions. *Nature* **2016**, *532*, 189–194.

(12) Wieder, B. J.; Bradlyn, B.; Wang, Z.; Cano, J.; Kim, Y.; Kim, H. S. D.; Rappe, A. M.; Kane, C. L.; Andrei Bernevig, B.Wallpaper Fermions and the Nonsymmorphic Dirac Insulator. *Science* **2018**, *361* (6399), 246–251.

(13) Bian, G.; Chang, T.-R.; Sankar, R.; Xu, S.-Y.; Zheng, H.; Neupert, T.; Chiu, C.-K.; Huang, S.-M.; Chang, G.; Belopolski, I.; Sanchez, D. S.; Neupane, M.; Alidoust, N.; Liu, C.; Wang, B.; Lee, C.-C.; Jeng, H.-T.; Zhang, C.; Yuan, Z.; Jia, S.; Bansil, A.; Chou, F.; Lin, H.; Hasan, & M. Z.Topological Nodal-Line Fermions in Spin-Orbit Metal

$PbTaSe_2$. *Nat. Commun.* **2016**, *7*, 10556.

(14) Lv, B. Q.; Weng, H. M.; Fu, B. B.; Wang, X. P.; Miao, H.; Ma, J.; Richard, P.; Huang, X. C.; Zhao, L. X.; Chen, G. F.; Fang, Z.; Dai, X.; Qian, T.; Ding, H.Experimental Discovery of Weyl Semimetal TaAs. *Phys. Rev. X* **2015**, *5*, 031013.

(15) Souma, S.; Wang, Z.; Kotaka, H.; Sato, T.; Nakayama, K.; Tanaka, Y.; Kimizuka, H.; Takahashi, T.; Yamauchi, K.; Oguchi, T.; Segawa, K.; Ando, Y.Direct Observation of Nonequivalent Fermi-Arc States of Opposite Surfaces in the Noncentrosymmetric Weyl Semimetal NbP. *Phys. Rev. B* **2016**, *93*, 161112.

(16) Xu, S. Y.; Belopolski, I.; Alidoust, N.; Neupane, M.; Bian, G.; Zhang, C.; Sankar, R.; Chang, G.; Yuan, Z.; Lee, C. C.; Huang, S. M.; Zheng, H.; Ma, J.; Sanchez, D. S.; Wang, B. K.; Bansil, A.; Chou, F.; Shibayev, P. P.; Lin, H.; Jia, S.; Hasan, M. Z.Discovery of a Weyl Fermion Semimetal and Topological Fermi Arcs. *Science* **2015**, *349* (6248), 613–617.

(17) Fu, B. B.; Yi, J.; Zhang, T. T.; Caputo, M.; Ma, J. Z.; Gao, X.; Lv, B. Q.; Kong, L. Y.; Huang, Y. B.; Richard, P.; Shi, M.; Strocov, V. N.; Fang, C.; Weng, H. M.; Shi, Y. G.; Qian, T.; Ding, H.Dirac Nodal Surfaces and Nodal Lines in ZrSiS. *Sci. Adv.* **2019**, *5* (5), eaau6459.

(18) Takane, D.; Wang, Z.; Souma, S.; Nakayama, K.; Trang, C. X.; Sato, T.; Takahashi, T.; Ando, Y.Dirac-Node Arc in the Topological Line-Node Semimetal HfSiS. *Phys. Rev. B*

2016, *94*, 121108.

(19) Hosen, M. M.; Dimitri, K.; Aperis, A.; Maldonado, P.; Belopolski, I.; Dhakal, G.; Kabir, F.; Sims, C.; Hasan, M. Z.; Kaczorowski, D.; Durakiewicz, T.; Oppeneer, P. M.; Neupane, M.Observation of Gapless Dirac Surface States in ZrGeTe. *Phys. Rev. B* **2018**, *97*, 121103.

(20) Hosen, M. M.; Dhakal, G.; Dimitri, K.; Maldonado, P.; Aperis, A.; Kabir, F.; Sims, C.; Riseborough, P.; Oppeneer, P. M.; Kaczorowski, D.; Durakiewicz, T.; Neupane, M.Discovery of Topological Nodal-Line Fermionic Phase in a Magnetic Material GdSbTe. *Sci. Rep.* **2018**, *8* (1), 13283.

(21) Wang, Y.; Qian, Y.; Yang, M.; Chen, H.; Li, C.; Tan, Z.; Cai, Y.; Zhao, W.; Gao, S.; Feng, Y.; Kumar, S.; Schwier, E. F.; Zhao, L.; Weng, H.; Shi, Y.; Wang, G.; Song, Y.; Huang, Y.; Shimada, K.; Xu, Z.; Zhou, X. J.; Liu, G.Spectroscopic Evidence for the Realization of a Genuine Topological Nodal-Line Semimetal in LaSbTe. *Phys. Rev. B* **2021**, *103*, 125131.

(22) Yen, Y.; Chiu, C. L.; Lin, P. H.; Sankar, R.; Chuang, T. M.; Guo, G. Y.Dirac Nodal Line and Rashba Spin-Split Surface States in Nonsymmorphic ZrGeTe. *New J. Phys.* **2021**, *23* (10), 103019.

(23) Li, S.; Liu, Y.; Wang, S.-S.; Yu, Z.-M.; Guan, S.; Sheng, X.-L.; Yao, Y.; Yang, S. A.Nonsymmorphic-Symmetry-Protected Hourglass Dirac Loop, Nodal Line, and Dirac

Point in Bulk and Monolayer Ta_3SiTe_6 (X = Ta, Nb). *Phys. Rev. B* **2018**, *97*, 045131.

(24) Ma, J.; Yi, C.; Lv, B.; Wang, Z.; Nie, S.; Wang, L.; Kong, L.; Huang, Y.; Richard, P.; Zhang, P.; Yaji, K.; Kuroda, K.; Shin, S.; Weng, H.; Bernevig, B. A.; Shi, Y.; Qian, T.; Ding, H.Experimental Evidence of Hourglass Fermion in the Candidate Nonsymmorphic Topological Insulator KHgSb. *Sci. Adv.* **2017**, *3*, e1602415.

(25) Li, J.; Badding, M. E.; DiSalvo, F. J.Synthesis and Structure of Nb_3SiTe_6, a New Layered Ternary Niobium Telluride Compound. *J. Alloys Compd.* **1992**, *184*, 257–263.

(26) Yang, T. Y.; Wan, Q.; Yan, D. Y.; Zhu, Z.; Wang, Z. W.; Peng, C.; Huang, Y. B.; Yu, R.; Hu, J.; Mao, Z. Q.; Li, S.; Yang, S. A.; Zheng, H.; Jia, J.-F.; Shi, Y. G.; Xu, N.Directional Massless Dirac Fermions in a Layered van Der Waals Material with One-Dimensional Long-Range Order. *Nat. Mater.* **2020**, *19*, 27–33.

(27) Sato, T.; Wang, Z.; Nakayama, K.; Souma, S.; Takane, D.; Nakata, Y.; Iwasawa, H.; Cacho, C.; Kim, T.; Takahashi, T.; Ando, Y.Observation of Band Crossings Protected by Nonsymmorphic Symmetry in the Layered Ternary Telluride Ta_3SiTe_6. *Phys. Rev. B* **2018**, *98*, 121111.

(28) Naveed, M.; Fei, F.; Bu, H.; Bo, X.; Shah, S. A.; Chen, B.; Zhang, Y.; Liu, Q.; Wei, B.; Zhang, S.; Guo, J.; Xi, C.; Rahman, A.; Zhang, Z.; Zhang, M.; Wan, X.; Song, F.Magneto-Transport and Shubnikov-de Haas Oscillations in the Layered Ternary Telluride Topological Semimetal Candidate Ta_3SiTe_6. *Appl. Phys. Lett.* **2020**, *116* (9),

92402.

(29) Hu, J.; Liu, X.; Yue, C. L.; Liu, J. Y.; Zhu, H. W.; He, J. B.; Wei, J.; Mao, Z. Q.; Yu Antipina, L.; Popov, Z. I.; Sorokin, P. B.; Liu, T. J.; Adams, P. W.; A Radmanesh, S. M.; Spinu, L.; Ji, H.Enhanced Electron Coherence in Atomically Thin Nb_3SiTe_6. *Nat. Phys.* **2015**, *11*, 471–476.

(30) An, L.; Zhang, H.; Hu, J.; Zhu, X.; Gao, W.; Zhang, J.; Xi, C.; Ning, W.; Mao, Z.; Tian, M.Magnetoresistance and Shubnikov-de Haas Oscillations in Layered Nb_3SiTe_6 Thin Flakes. *Phys. Rev. B* **2018**, *97*, 235133.

(31) Pang, Y.; Rezaei, E.; Chen, D.; Li, S.; Jian, Y.; Wang, Q.; Wang, Z.; Duan, J.; Zebarjadi, M.; Yao, Y.Thermoelectric Properties of Layered Ternary Telluride Nb_3SiTe_6. *Phys. Rev. Mater.* **2020**, *4*, 094205.

(32) Moser, S.An Experimentalist's Guide to the Matrix Element in Angle Resolved Photoemission. *J. Electron Spectros. Relat. Phenomena* **2017**, *214*, 29–52.

(33) Zhang, P.; Richard, P.; Qian, T.; Xu, Y.-M.; Dai, X.; Ding, H.A Precise Method for Visualizing Dispersive Features in Image Plots. *Rev. Sci. Instrum.* **2011**, *82*, 043712.

(34) Liang, S.; Kushwaha, S.; Gao, T.; Hirschberger, M.; Li, J.; Wang, Z.; Stolze, K.; Skinner, B.; Bernevig, B. A.; Cava, R. J.; Ong, N. P.A Gap-Protected Zero-Hall Effect State in the Quantum Limit of the Non-Symmorphic Metal KHgSb. *Nat. Mater.* **2019**, *18*, 443–447.

FIGURE CAPTIONS

Figure 1. Atomic lattice structure and characterizing hourglass bands in Nb_3SiTe_6. (a) Atomic structure of Nb_3SiTe_6. (b) Bulk BZ and (001)-projected surface BZ (gray rectangle). (c) Topographic image of an *in situ* cleaved Nb_3SiTe_6 surface (V_s = -100 mV, I_t = 1500 pA, 10×10 nm^2, T = 4.2 K). The inset is the corresponding Fast Fourier Transform (FFT) of the topographic image. In the inset, the red rectangle marks the [001]-projected SBZ, while yellow circles indicate Bragg peaks from Te atoms in the topmost layer. (d) DFT band structure of Nb_3SiTe_6. Here, the label α and red arrows identify hourglass band dispersions along the XS *k*-path near the Fermi level, while hourglass bands gapped by SOC along YΓZ close to the Fermi level are marked by the label β and a green arrow; the label γ and yellow arrows indicate hourglass bands at deeper binding energies, and the label s and blue arrows flag bands which form a saddle-shaped surface centered about the Γ point in energy-momentum space. (e) Panoramic view of the constant energy contours of Nb_3SiTe_6 in the first BZ (FBZ). (f) Schematic diagrams for the nodal loop in the XSRU plane (left, red oval) and band structures of the hourglass dispersion 1 (HD1) and hourglass dispersion 2 (HD2) along SXΓ (right) that give rise to the nodal loop. The nodal loop is formed by the band crossing points (red and yellow points in the right panel).

Figure 2. Fermi surface and band mappings of Nb_3SiTe_6. (a) Fermi surface map of Nb_3SiTe_6. Here, the result is obtained by integrating the ARPES intensity within ±10 meV of the Fermi level. Solid black lines correspond to BZ boundaries, where the lengths of $\overline{\Gamma X}$ and $\overline{\Gamma Y}$ are 0.48 $Å^{-1}$ and 0.26 $Å^{-1}$, respectively; the first BZ is at the top left corner (labelled FBZ), while strategically chosen momentum cuts used for obtaining ARPES band mappings are indicated by colored arrows. (b), (c) Measured band maps along cuts 1 and 2 in the Fermi surface map of (a), respectively [red and orange arrows in (a)]; both momentum cuts are parallel to $\overline{\Gamma Y}$. (d),(e) Experimental ARPES spectra along cuts 3 and 4 in the Fermi surface map of (a), respectively [green and blue arrows in (a)]; both momentum cuts are parallel to $\overline{\Gamma X}$, and the fat blue and aqua arrows in (e) identify two sets of Dirac-like, linear band crossings. In all mappings here, the incident photon energy is 60 eV.

Figure 3. Candidate nodal loop bands before and after alkali-metal doping along $\overline{\Gamma Y}$. (a) Band structure along cut 2 in Fig. 2(a) obtained using 60-eV photons; the mapping is overlaid with DFT results (red solid lines), and a nodal loop band structure (green arrow and label β) and the saddle-shaped surface (blue arrow and label s) are identified. (b),(c) 2D curvature results for band mappings along $\overline{\Gamma Y}$ before and after K doping, respectively, each taken using an incident photon energy of 100 eV and superimposed with DFT band structures (red solid lines). In (c), a band whose intensity is enhanced after K doping is identified (red arrow), and bands corresponding to the saddle-shape surface (blue arrow and label s) and the hourglass bands gapped by SOC (green arrow and label β) are indicated.

Figure 4. Constant energy contour maps and potential double QSH state in Nb_3SiTe_6. (a) BZ and the schematic band structures (blue and aqua lines) of hourglass fermions and their partner linear subbands along the SXΓ *k*-path. (b),(c) Constant energy contour maps in the FBZ and band mapping along $\overline{\Gamma X}$, respectively, all taken using 70-eV photons. The integrated energy range in each map is 25 meV; in (b) and (c), aqua and blue arrows indicate two sets of linear bands near each of the $\overline{X}$ points, while in (b), the red solid arrow indicates a momentum cut corresponding to the ARPES spectra in (c). (d) Spin-resolved DFT band structures for the two linear band crossings at the $\overline{X}$ point with spin-polarization projection taken along the k_y-direction or $\overline{\Gamma Y}$. (e) Fermi surface mapping in the k_x-k_z plane obtained by integrating the ARPES intensity within ±25 meV of the Fermi level, where k_x and k_z are momentum components parallel to the $\overline{\Gamma X}$ and [001] directions, respectively; BZ boundaries are labelled along the left axis and/or identified by black lines.

Figure 5. k_z-dependent band mappings of hourglass fermion dispersions. (a) DFT band structure results along the XS *k*-path; the nodal point of the hourglass fermion in the middle of XS is marked by a red arrow, and the dashed red rectangles identify both the BZ boundaries and possible regions of interest for k_z-dependent mappings of hourglass bands near the Fermi level. (b) 2D curvature map corresponding to the k_z-dependent spectra taken at the $\overline{\mathrm{X}}$ point; here, k_z is varied from around 4.0 to 4.5 Å^{-1}. (c) Similar to (b) but for k_z taken from around 4.5 to 5.0 Å^{-1}. (d)–(g) 2D curvature band mappings along $\overline{\Gamma\mathrm{X}}$ measured near $\overline{\mathrm{X}}$ for k_z = 4.0, 4.23, 4.5, and 4.7 Å^{-1}, respectively.

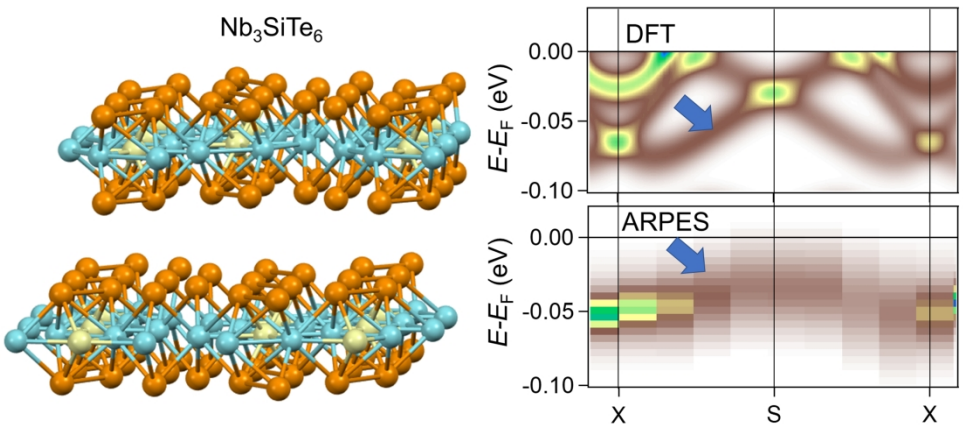

Table of Contents Graphic

369x180mm (300 x 300 DPI)

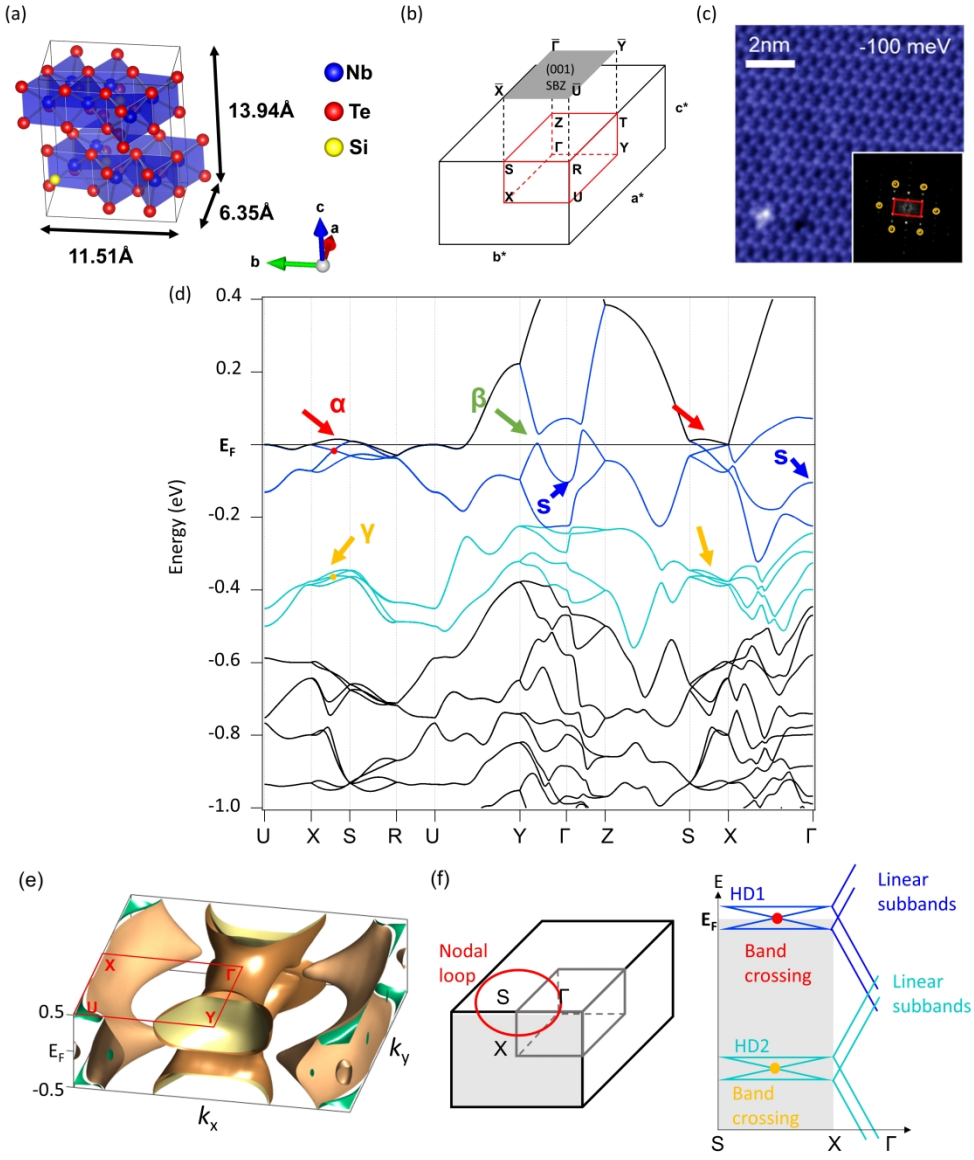

Figure 1.

309x369mm (300 x 300 DPI)

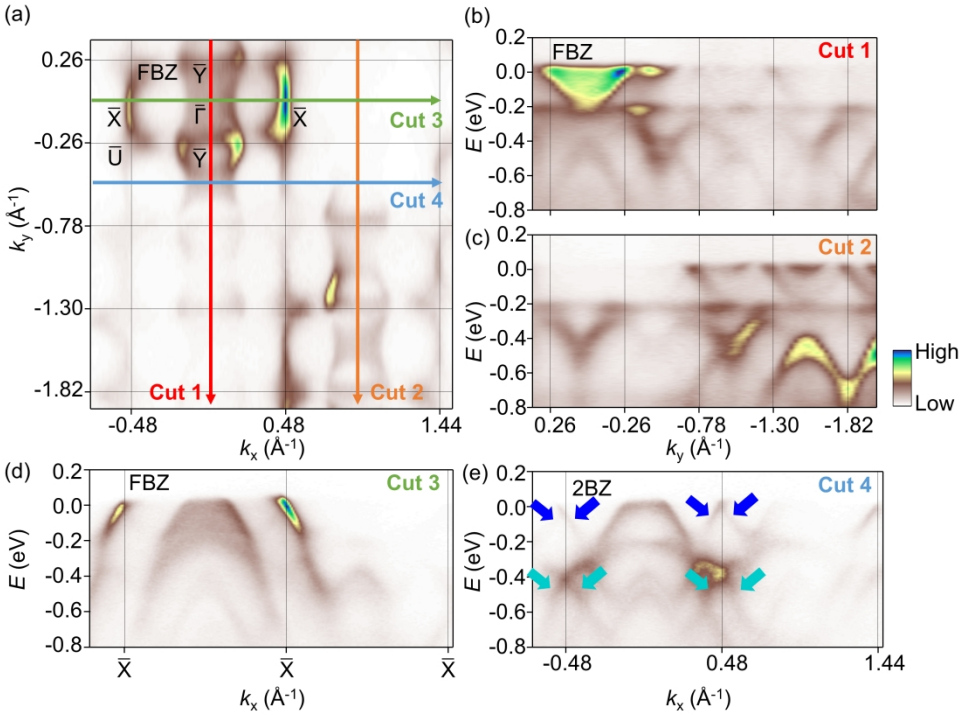

Figure 2.

294x219mm (300 x 300 DPI)

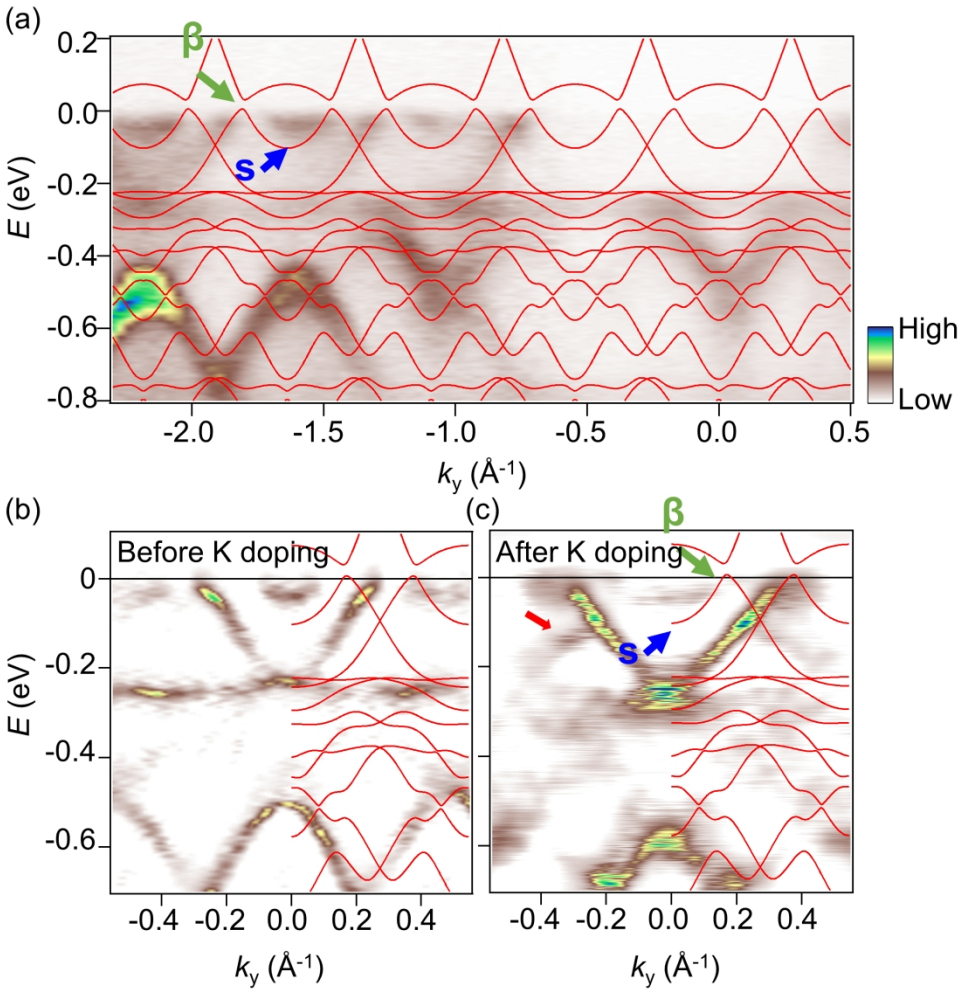

Figure 3.

215x219mm (300 x 300 DPI)

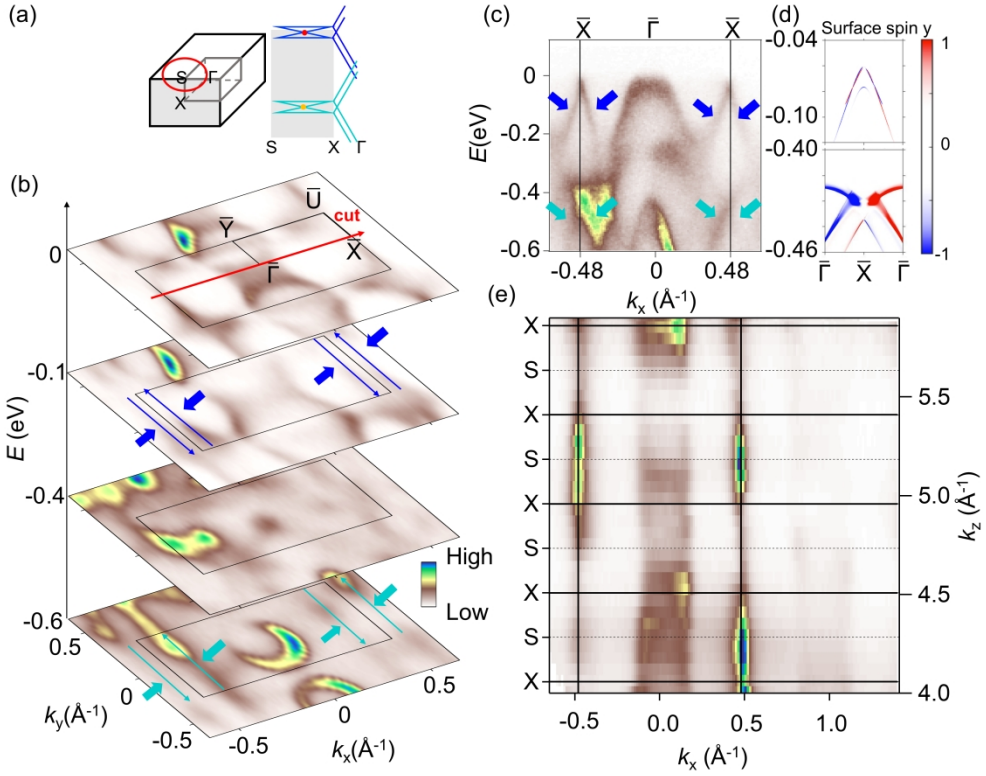

Figure 4.

365x305mm (300 x 300 DPI)

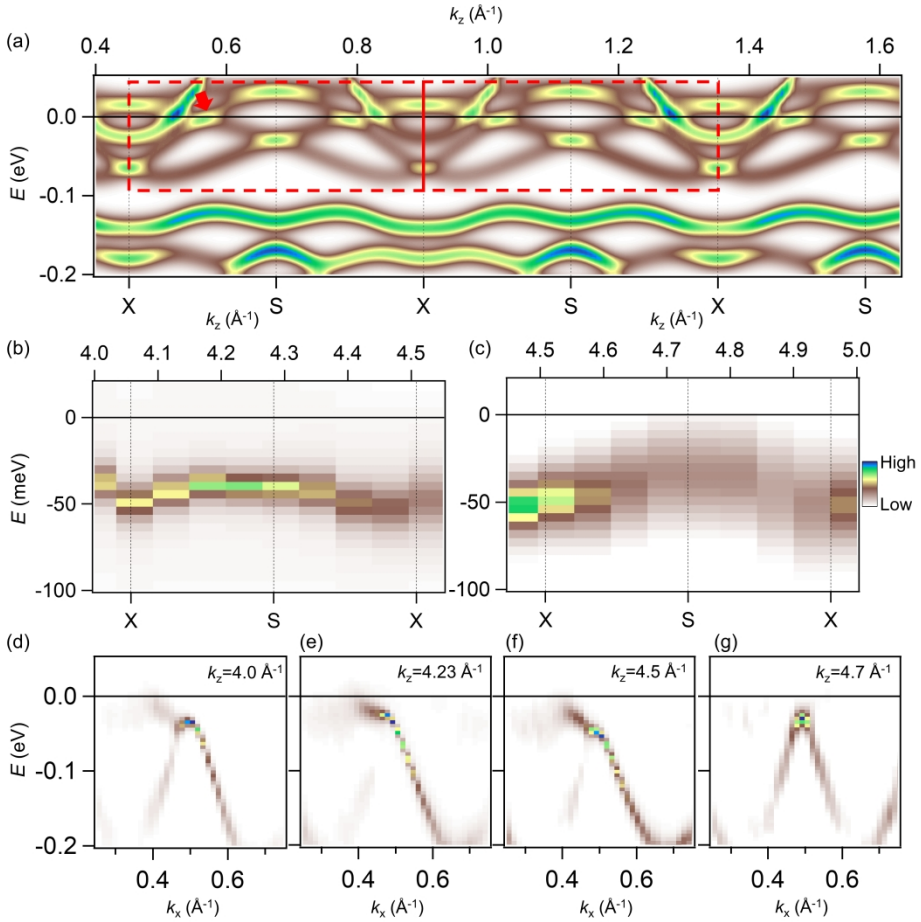

Figure 5.

363x345mm (300 x 300 DPI)